RESEARCH ARTICLE

Improving motion robustness of 3D MR fingerprinting with a fat navigator

Siyuan Hu[1] | **Yong Chen**[2] | **Xiaopeng Zong**[3] | **Weili Lin**[4] | **Mark Griswold**[2] |
Dan Ma[1]

[1]Department of Biomedical Engineering, Case Western Reserve University, Cleveland, Ohio, USA

[2]Department of Radiology, Case Western Reserve University, Cleveland, Ohio, USA

[3]School of Biomedical Engineering, ShanghaiTech University, Shanghai, China

[4]Department of Radiology, University of North Carolina, Chapel Hill, North Carolina, USA

Correspondence
Dan Ma, Department of Biomedical Engineering, Case Western Reserve University, 11100 Euclid Ave. Bolwell Building B110, Cleveland, OH 44106, USA.
Email: dan.ma@case.edu

Purpose: To develop a 3D MR fingerprinting (MRF) method in combination with fat navigators to improve its motion robustness for neuroimaging.

Methods: A rapid fat navigator was developed using the stack-of-spirals acquisition and non-Cartesian spiral GRAPPA. The fat navigator module was implemented in the 3D MRF sequence with high scan efficiency. The developed method was first validated in phantoms and five healthy subjects with intentional head motion. The method was further applied to infants with neonatal opioid withdrawal symptoms. The 3D MRF scans with fat navigators acquired with and without acceleration along the partition-encoding direction were both examined in the study.

Results: Both phantom and in vivo results demonstrated that the added fat navigator modules did not influence the quantification accuracy in MRF. In combination with non-Cartesian spiral GRAPPA, a rapid fat navigator sampling with whole-brain coverage was achieved in ~0.5 s at 3T, reducing its sensitivity to potential motion. Based on the motion waveforms extracted from fat navigators, the motion robustness of the 3D MRF was largely improved. With the proposed method, the motion-corrupted MRF datasets yielded T1 and T2 maps with significantly reduced artifacts and high correlations with measurements from the reference motion-free MRF scans.

Conclusion: We developed a 3D MRF method coupled with rapid fat navigators to improve its motion robustness for quantitative neuroimaging. Our results demonstrate that (1) accurate tissue quantification was preserved with the fat navigator modules and (2) the motion robustness for quantitative tissue mapping was largely improved with the developed method.

KEYWORDS
fat navigator, magnetic resonance fingerprinting, motion correction, relaxometry, spiral GRAPPA

1 | INTRODUCTION

Subject motion is ubiquitous in clinical imaging and presents one of the major challenges for MR imaging of children, as well as for patient populations such as Parkinson's patients and stroke patients.[1] Compared to conventional MR imaging, MR fingerprinting (MRF) enables efficient and simultaneous quantification of multiple tissue parameters (T1, T2, and spin density) in one acquisition with promising robustness against motion.[2] MRF uses pseudorandomized acquisition parameters to encode MR signals and generates tissue properties of interest using a template matching algorithm based on a pre-defined MRF dictionary. MRF often utilizes non-Cartesian trajectories for spatial encoding, which is known to generally exhibit more benign artifacts in the presence of motion. The template matching algorithm used to extract quantitative tissue properties also provides another route to reduce motion artifacts.[3] The original 2D MRF paper demonstrated that accurate quantification and motion-artifacts-free maps could still be made, despite 20% of subject motion during scanning.[2] However, recent studies have shown that motion tolerance in MRF depends on the magnitude and timing of motion along the whole acquisition.[4,5] Simply relying on non-Cartesian sampling and the inherent error tolerance of template matching is often insufficient to eliminate motion effects, causing image blurriness and measurement errors in quantitative maps.[6] This limitation is further amplified for 3D MRF scans with volumetric coverage due to the prolonged scan time (typically around 5–10 min).

To further improve the motion robustness of MRF scans, retrospective motion correction algorithms based on motion estimation extracted from MRF measurements have been developed for 2D MRF.[4,5,7] Mehta et al.[4] proposed to estimate and compensate for motion iteratively via pattern recognition and image registration to improve data consistency during image reconstruction. However, it is challenging for image-registration-based methods to accurately estimate motion from highly undersampled MRF data, where the image from each time frame is acquired with only one single spiral interleaf. Instead, other studies proposed extracting motion signals from dynamic image series with reduced aliasing artifacts obtained from sliding-window reconstructions, and motion corrections were directly performed in k-space.[5,7] While these methods work effectively for in-plane motion, they typically face technical challenges in correcting through-plane motion as proton signals moving in and out of image slices are difficult to be included in the modeling.[4] 3D MRF acquisitions allow potential corrections of both in-plane and through-plane motions, since all the proton signals in the 3D imaging slab are excited.

To reduce the effect of bulk motion in 3D MRF, Kurzawski et al.[8] adopted the self-navigation strategy similar to the method implemented for 2D MRF for motion detection. Data acquired from each segment block were combined to obtain a volumetric dataset, which were co-registered to extract motion signals, followed by motion corrections in k-space. Pirkl et al.[9] also used this approach to estimate motion signals in scans but applied convolutional neural networks to improve the latter motion correction step. In these studies, motion estimation was sensitive to the image quality of intermediate images, which could be affected by the designs of sampling trajectories of MRF scans, the spatial information encoded in each segment, and the algorithm to realign intermediate image volumes.

While the majority of MRF motion correction studies for neuroimaging focused on extracting motion information from MRF signals by taking advantage of the temporal correlations of intermediate images, navigator-based motion correction was not yet investigated. As compared to the self-navigation methods, navigator-based motion detection relies on additionally acquired data and the accuracy of motion estimation is independent of the image quality of intermediate images. Recently, motion navigation using the magnetization signal from subcutaneous fat around the skull has been proposed for neuroimaging.[10–12] Comparing to water-signal-based navigators, excitation of fat signal by fat-selective RF pulse yields minimal perturbation to imaging signals. Additionally, due to the sparse distribution of subcutaneous fat in the image domain, the acquisition of fat navigator images can be highly accelerated with parallel imaging to achieve a high scan efficiency.[10] Motion correction methods based on 3D fat images were previously developed to correct motion artifacts in structural brain imaging.[13] In the original implementation, low-resolution fat images with whole brain coverage can be achieved in approximately 1.2 s with a high GRAPPA acceleration factor of 16 (4 by 4) along both phase-encoding and slice-encoding directions.[14] When combined with the MPRAGE acquisition, the fat navigator module is acquired before inversion pulses during the waiting time.

In this study, we aimed to improve the motion robustness of 3D MRF scans by using 3D fat navigators. The fat navigators were acquired during the waiting time at the end of each partition acquisition of 3D MRF, so the total scan time remained the same. Motions in six degrees of freedom were estimated through image registration of the acquired 3D fat images from each partition with a 7 s temporal resolution. MRF data were then corrected in k-space by rotation of trajectory coordinates and phase shifting of acquired signals. We first studied the accuracy of motion estimation using the fat navigators with different GRAPPA

acceleration factors. Then, we identified the acquisition scheme achieving the most appropriate accuracy and scan efficiency and implemented the scheme in the following in vivo scans. The 3D MRF protocol integrated with the accelerated fat navigator modules was validated on healthy volunteers. Additionally, the effect of various motion artifacts on the accuracy and image quality of 3D MRF was investigated in both simulations and in vivo experiments.

2 | METHODS

2.1 | 3D MRF sequence with fat navigator

The 3D MRF method was designed based on the prior study by Ma et al.[15,16] that utilized a stack-of-spirals acquisition. Specifically, the 3D MRF dataset was acquired along the partition direction (axial direction) with linear ordering.[17] A 2-s waiting time was applied at the end of each partition acquisition for partial signal recovery. The same acquisition parameters, including the flip angle, TR patterns, and in-plane spiral readouts, were repeated for each partition in the 3D scan. Each MRF time frame was highly undersampled by acquiring one spiral interleaf per partition, with an undersampling factor of 48.[2] Imaging parameters included: $FOV = 300 \times 300 \times 144 \, mm^3$; matrix size = $256 \times 256 \times 144$; number of MRF time frame = 480; undersampling factor along partition direction = 3; scan time = 5.6 min.

A fat navigator was inserted during the 2-s waiting time at the end of each partition acquisition (Figure 1A).[13] The fat navigator was designed based on a 3D FLASH sequence with a 1-2-1 binomial RF pulse for fat excitation. Compared to the previous implementation of fat navigators at 7T, the chemical shift between fat and water is reduced from approximately 1000 to 440 Hz at 3T. This reduction increases the duration of fat excitation pulses (approximately 3.3 ms) and by extension, the total acquisition time for each fat navigator module. To accelerate the 3D fat navigator and minimize the sensitivity of the navigator itself to motion, standard Cartesian sampling was replaced with a stack-of-spirals trajectory.[18,19] A total of 24 spiral arms were used to acquire the data in-plane. The fat navigator acquisition was further accelerated using the spiral GRAPPA technique along both in-plane and through-plane directions (Figure 1B). To calibrate the GRAPPA weights for the accelerated fat navigator, a calibration scan including one fully-sampled volume was first acquired in 9.7 s before all the scans. Other imaging parameters for the fat navigator modules included:

$FOV = 250 \times 250 \times 144 \, mm^3$; matrix size = $128 \times 128 \times 48$; TE/TR = 3.7/8.4 ms; flip angles = 6°.

All measurements were performed on Siemens 3T Skyra and Vida scanners using a 20-channel head coil (Siemens Healthineers, Erlangen, Germany).

2.2 | Motion estimation

The Fat navigator image acquired at the end of each partition was separately reconstructed. For accelerated fat navigator acquisitions using spiral GRAPPA, each fat image volume was reconstructed with a 3×2 GRAPPA kernel in both directions (Figure 1B)[20] followed by NUFFT.[21] Translational (x, y, z) and rotational (φ1, φ2, φ3) motions were extracted from co-registering the reconstructed fat navigator volumes using the SPM12 toolbox (Statistical Parametric Mapping).[22] The fat image acquired right after the acquisition of the central k-space partition in a 3D MRF scan was used as the reference to compute the relative motion waveforms. Motion signals were measured every 7 s, corresponding to the acquisition time for one partition including ∼5 s of MRF data sampling and the 2-s waiting time.

To evaluate the accuracy of motion estimation of the accelerated fat navigator and identify the appropriate parameters for combined in-plane and through-plane accelerations of fat navigator acquisitions using spiral GRAPPA, a retrospective undersampling experiment was performed with an in vivo scan. Specifically, a 3D MRF scan was acquired on a normal volunteer with each fat navigator volume fully sampled during the scan. In this case, the scan time of the 3D MRF was extended to 12.8 min due to the prolonged waiting time, while the actual 3D MRF scans implemented with accelerated fat navigator acquisitions took 5.6 min. The subject was instructed to change the head position 5 to 10 times during the scan while staying still in between movements. In this experiment, the fully sampled fat navigators were first reconstructed by direct NUFFT[21] to extract the reference motion signals. The fat navigator data were then retrospectively undersampled with various combinations of in-plane (R = 6 or 8) and through-plane (R = 2 or 3) reduction factors and reconstructed based on the method mentioned above. The motion waveforms measured from different acceleration schemes were compared to the reference motion signals. The optimal GRAPPA factor combinations were determined based on the mean differences of the measured motion signals as well as scan times. The accelerated fat navigators with the chosen settings of acceleration factors were implemented in the later validation experiments.
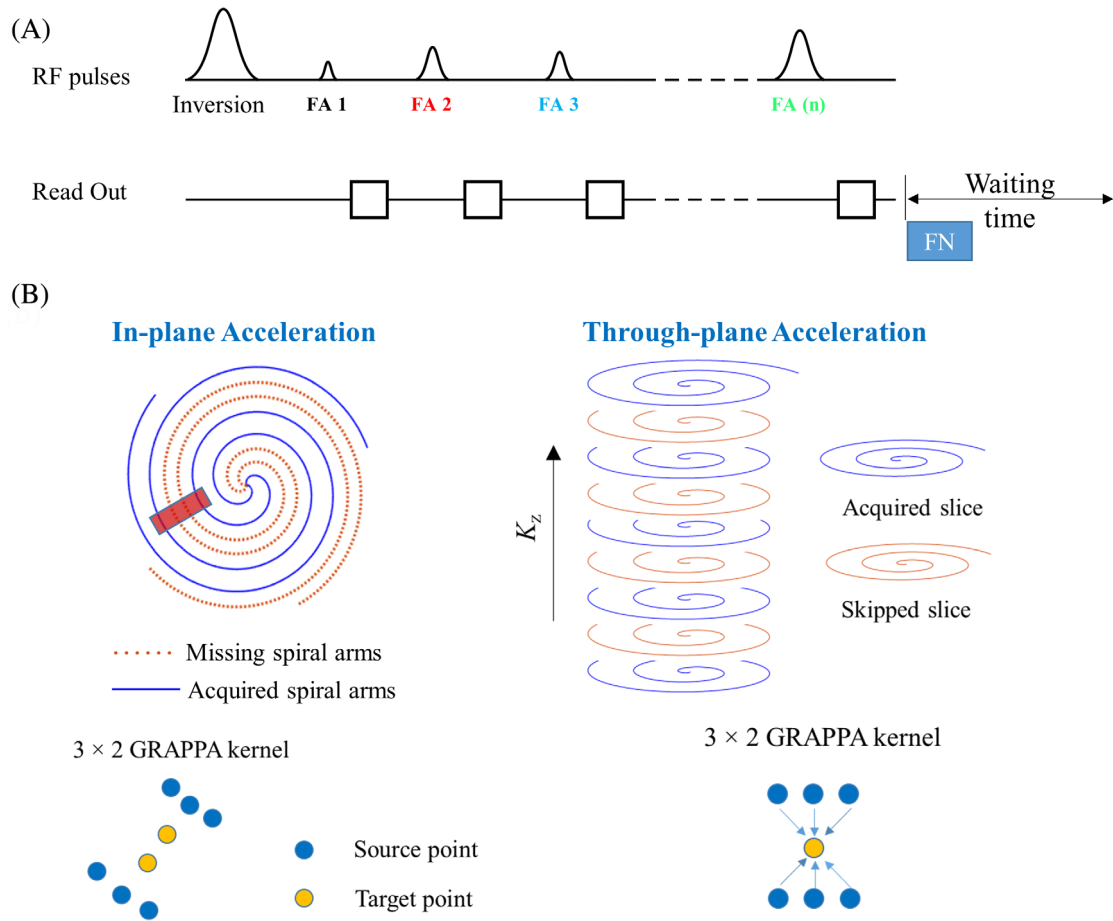
FIGURE 1 (A) Diagram of 3D MRF with fat navigator (FN). The navigator module was applied at the end of MRF data acquisition for each partition. (B) Illustration of GRAPPA reconstruction for spiral trajectory. This was applied to accelerate both in-plane and through-plane acquisition of fat navigator. A 3×2 GRAPPA kernel was used in the study to fill out the missing points.

2.3 | Motion correction

The 3D MRF data were corrected in k-space using the extracted motion signals before MRF reconstruction. Based on Fourier transform properties, a translation in the image domain corresponds to a linear phase shift of k-space data and a rotation in the image domain causes the same rotation in k-space. The motion-corrected k-space signal $S_{corrected}$ is given by:

$$S\left(\mathbf{R}^{-1}\hat{k}\right)_{corrected} = S(\hat{k})_{raw}e^{-i2\pi\hat{k}\mathbf{v}}$$

where S_{raw} is the motion-corrupted k-space signal sampled along the trajectory $\hat{k}$, $\mathbf{R}$ is the rotational matrix with the corresponding rotational angle, and $\mathbf{v}$ is the translation vector. The 3D MRF data were corrected partition by partition. Specifically, the k-space data from each partition were corrected using the motion parameters estimated from the fat navigator acquired right after the corresponding partition.

2.4 | MRF reconstruction

The 3D MRF datasets after motion correction were processed using an iterative reconstruction method with singular value decomposition (SVD)-based dictionary compression.[23,24] Nine SVD images were extracted for iterative reconstruction, where the relative errors between the k-space of the reconstructed images and the raw k-space data were minimized using nonlinear conjugate gradient descent.[24] To be noted, the 3D NUFFT kernel and density compensation coefficients of the spiral trajectories used in the MRF reconstruction were calculated using the new trajectories obtained after motion correction. The signal evolution from each voxel on the reconstructed images was matched to a pre-defined MRF dictionary to extract quantitative T1 and T2 relaxation times. The MRF dictionary was generated using Bloch equation simulations with the actual acquisition parameters. A total of approximately 15 000 entries are contained in the MRF dictionary, covering a wide range of T_1 (2–4000 ms) and T_2 (2–2000 ms) values. The image reconstruction was performed offline

on a standalone workstation (12 core, 2.6 GHz Intel Xeon E5-2630 v2 processor; and 128 GB RAM).

2.5 | Validations

The 3D MRF with accelerated fat navigator was validated in several experiments. First, we evaluated the accuracy of T1 and T2 measurements of the 3D MRF with fat navigator acquisitions in both phantom and in vivo experiments without motion. Second, we performed simulations to investigate how motion impacts the image quality and quantitative accuracy of 3D MRF and to evaluate the performance of the motion correction algorithm. Third, in vivo scans were acquired on healthy volunteers and a pediatric subject using the fat-navigated 3D MRF to validate the motion robustness of the proposed method.

2.5.1 | Measurement accuracy of MRF with fat navigator

The quantitative accuracy of the 3D MRF scan incorporated with accelerated fat navigator acquisitions was validated on both phantom and a healthy subject without motion. For the phantom study, a NIST phantom was scanned using the 3D MRF protocol with and without fat navigator modules applied in two separate scans. The in vivo experiment was conducted similarly to the phantom scans, where 3D MRF scans were acquired from a volunteer with and without the application of fat navigators. The volunteer was asked to stay as still as possible during the two MRF scans. T1 and T2 measurements from the fat-navigated MRF scan were compared to the MRF scan without fat navigator to evaluate the impact of fat navigator on quantitative accuracy.

2.5.2 | Simulations

Simulations were performed to evaluate the effect of motion on the image quality and measurement accuracy of 3D MRF before and after motion correction. A digital brain phantom with realistic T1, T2, and proton density values was used to simulate acquisitions according to the actual 3D MRF scheme. Simulated motion was applied to the simulated image series in the image domain. The data were then undersampled and the motion was corrected in k-space. The motion-corrected data were then reconstructed into T1 and T2 maps using the low-rank iterative algorithm as described in the image reconstruction section. Three simulation studies were conducted to explore the effect of applying (1) various types of motion, (2) motion at various timings during the scan, and (3)

motion patterns acquired from actual in vivo scans. In the first study, four types of sinusoidally varying motion waveforms were simulated (Figure S1A): in-plane rotation, through-plane rotation, in-plane translation, and through-plane translation. In the context of this study, in-plane motion indicates motion within the x-y plane, and through-plane describes motion in the x-z and y-z planes. For the second study, 3D motion was applied to the first (partition 1–48), the middle (partition 49–96), and the last (partition 97–144) part of acquisitions respectively (Figure S1B). The simulated rotational motions were within ±10° and the translational motions were within ±5 mm to mimic the worst-case scenario, matching the extent of motion observed during in vivo scans (Figure 5A). The last study was to obtain a simulation as similar to in vivo scenarios as possible, where a motion waveform extracted from a preliminary in vivo scan, rather than the synthetic sinusoidal waveform was applied. (Figure S1C).

2.5.3 | In vivo experiments

All in vivo experiments were conducted with approval from the Institutional Review Board. Informed consent was obtained from all volunteers after the nature of the procedures had been fully explained before the MRI scans. To test the motion robustness of the proposed 3D MRF scan with accelerated fat navigator acquisitions, five normal volunteers were scanned with intentional motions. All subjects were scanned with a reference MRF scan with no motion and three MRF scans with three types of motions. The volunteers were instructed to perform shaking (in x-y plane, left–right direction), nodding (in y-z plane, up-down direction), and rolling motions (in x-z plane, left–right direction) by changing head positions during the MRF acquisition waiting time in three separate scans (approximately moving every 10 to 20 s). The volunteers were asked to reach the maximum range of head movements allowed in the head coil for each motion type. One volunteer was scanned with additional three scans to test the robustness of the 3D MRF when motions were present during different time intervals of the acquisitions. Similar to the simulations, the volunteer intentionally performed shaking motion in the first, middle, and last 30% of the scans. We also compared the motion robustness of the fat-navigated MRF scan and conventional MR scans in additional in vivo scans (see more details in Supplementary Materials).

2.6 | Data analysis

Region-of-interested (ROI) analysis was performed on the phantom and in vivo experiment data obtained in

Section 2.5.1. For the phantom data, mean T1 and T2 relaxation values of each phantom tube obtained from the MRF scan with and without fat navigator were compared with each other. Mean percentage differences of T1 and T2 of all phantom tubes obtained from the fat-navigated and the navigator-free MRF scans were calculated. The in vivo MRF maps were also analyzed similarly. ROIs were drawn on frontal white matter, putamen, and thalamus (Figure S2A) to extract quantitative tissue properties from the two MRF scans for comparison.

In all simulation studies (Section 2.5.2), the simulated T1 and T2 maps were compared against the ground truth phantom maps to obtain percentage RMS errors between the corrected and non-corrected MRF maps and ground truth.

To evaluate the image quality of the in vivo MRF scans acquired in Section 2.5.3, the motion-corrected and non-corrected MRF maps were compared against the reference motion-free MRF datasets by pixel-wise quantitative analysis for all volunteer data. Specifically, the MRF maps from the motion scans and the reference scans were skull stripped and co-registered. T1 and T2 values of the center slice were compared pixel-wise. The intra-class correlation coefficient (ICC) was calculated to indicate the similarity between each pair. To evaluate the quantification accuracy of the MRF scans after motion

correction, ROI-based comparisons of T1 and T2 values between the motion-corrected MRF maps and the reference MRF maps were also performed. Example ROIs of white matter and gray matter drawn on a representative volunteer are presented in Figure S3. Mean and SDs of the T1 and T2 values measured with shaking, nodding, and rolling motions were calculated across all volunteers.

3 | RESULTS

3.1 | Determining acceleration scheme for fat navigators

Figure 2 shows the results of different acceleration schemes applied in reconstructing fat navigator images using spiral GRAPPA. This was based on an in vivo dataset acquired with fully-sampled fat navigator samples. Representative motion waveforms extracted with an in-plane acceleration factor of 6 and a through-plane acceleration of 3 (R6-3) were plotted for all six motion parameters in Figure 2A. The reference waveforms obtained from fat navigator images without any acceleration are also presented for comparison. A total of four acceleration schemes were evaluated in Figure 2B showing the differences in motion measurement for each
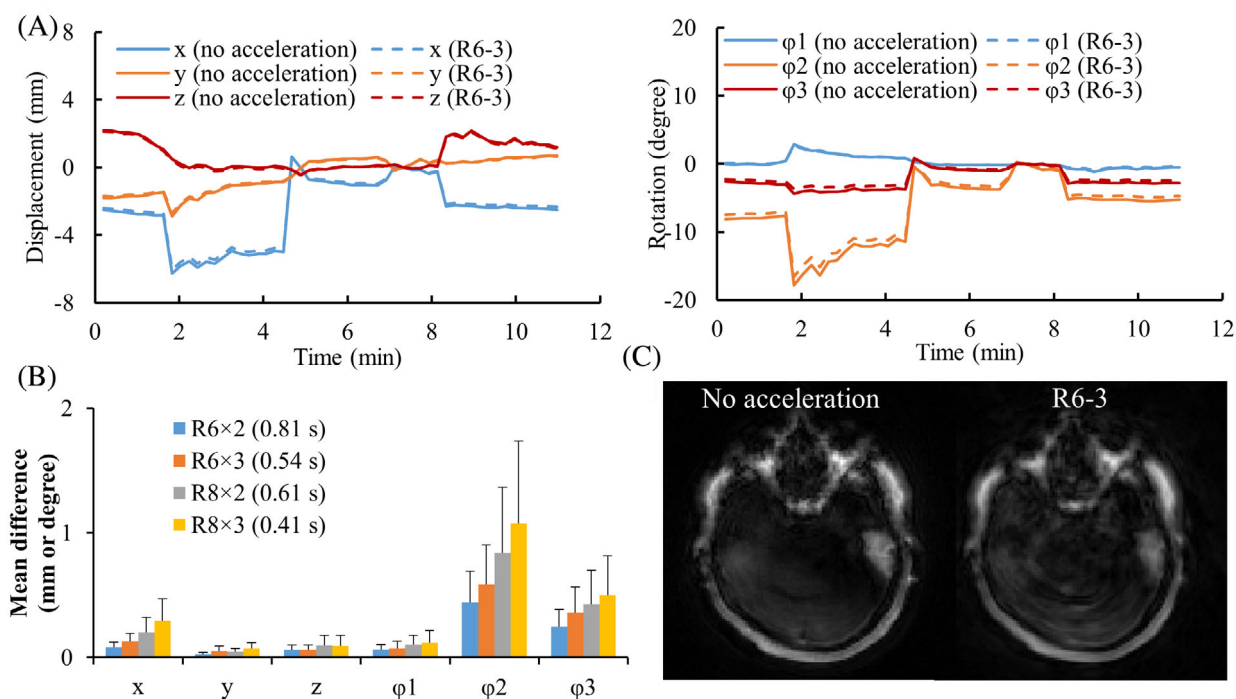

FIGURE 2 Optimization of the acceleration scheme for fat navigator. (A) Motion curves obtained in the scan. The results obtained with an in-plane reduction factor of 6 and through-plane factor of 3 (R6 × 3) are shown along with the reference curves (no acceleration). (B) Mean differences across all the navigators acquired in one scan. The scan time for one module is presented. Based on the results, R6 × 3 was selected for the following tests (~0.5 s per module). (C) Representative fat images.

acceleration scheme. The scan times needed to acquire one fat navigator with the corresponding acceleration schemes are also listed. It varies from 0.41 s per fat navigator module (R8-3) to 0.81 s (R6-2), all of which fit in the 2-s waiting period. Among the four acceleration schemes, the combined in-plane and through-plane acceleration of R6×3 could achieve measurement differences smaller than 1 degree/1 mm at the shortest acquisition time. Therefore, R6×3 within was selected in the following in vivo study (approximately 0.5 s acquisition time per fat navigator module). A representative fat navigator image reconstructed based on the data acquired using this acceleration scheme is shown in Figure 2C. In the actual in vivo studies, acquisition of the extra fat navigator data does not increase the scan time of 3D MRF, only a calibration scan of 9.7 s is needed before the 3D MRF scan.

3.2 | Impact of adding fat navigator on the measurement accuracy of MRF

Figure 3 shows the phantom results obtained with and without the fat navigator. Both quantitative maps and results from the ROI analysis are presented. A good agreement was observed in both T1 and T2 values with an average percentage difference of $2.4 \pm 1.4\%$ for T1 and $1.8 \pm 1.4\%$ for T2, which were within the intra-scanner measurement variance of T1 and T2 reported in a prior reproducibility study.[25] Similar findings were obtained with the in vivo experiment (Figure S2), where the T1 and T2 values measured with and without the fat navigator were consistent in all ROIs. The residual differences might also come from the imperfect excitation profile of the fat-selective RF pulse, where the water signals in the phantom were partially affected. Both the phantom and in vivo results suggest the application of fat navigators during the waiting period hardly influences the accuracy of tissue quantification based on water signal in the MRF acquisitions.

3.3 | Motion simulations

Figure 4 shows the simulation results of the 3D MRF scans obtained with and without motion correction in the three simulation studies. The simulated T1 and T2 maps and their corresponding error maps compared against the reference brain phantom maps are presented. Figure 4A shows the results of applying four types of motion in the acquisitions. Rotational motion mainly caused blurring of sharp edges, while translational motion led to both blurring and ghosting artifacts without motion corrections on
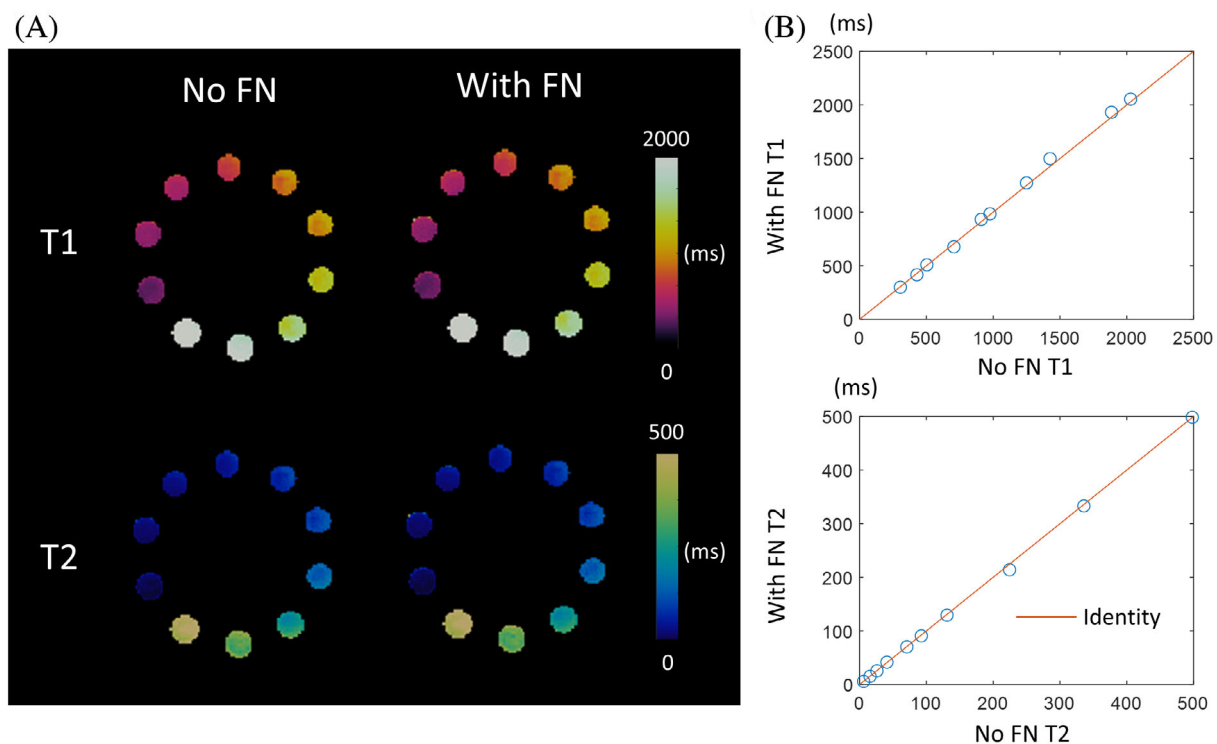

FIGURE 3 Phantom validation. (A) T1 and T2 maps obtained with and without the fat navigator module applied during the 3D MRF acquisition. (B) Correlation of the relaxation times obtained from the two methods. Compared to the standard 3D MRF method without the application of fat navigator modules, a good agreement was observed from the results obtained with the proposed method.
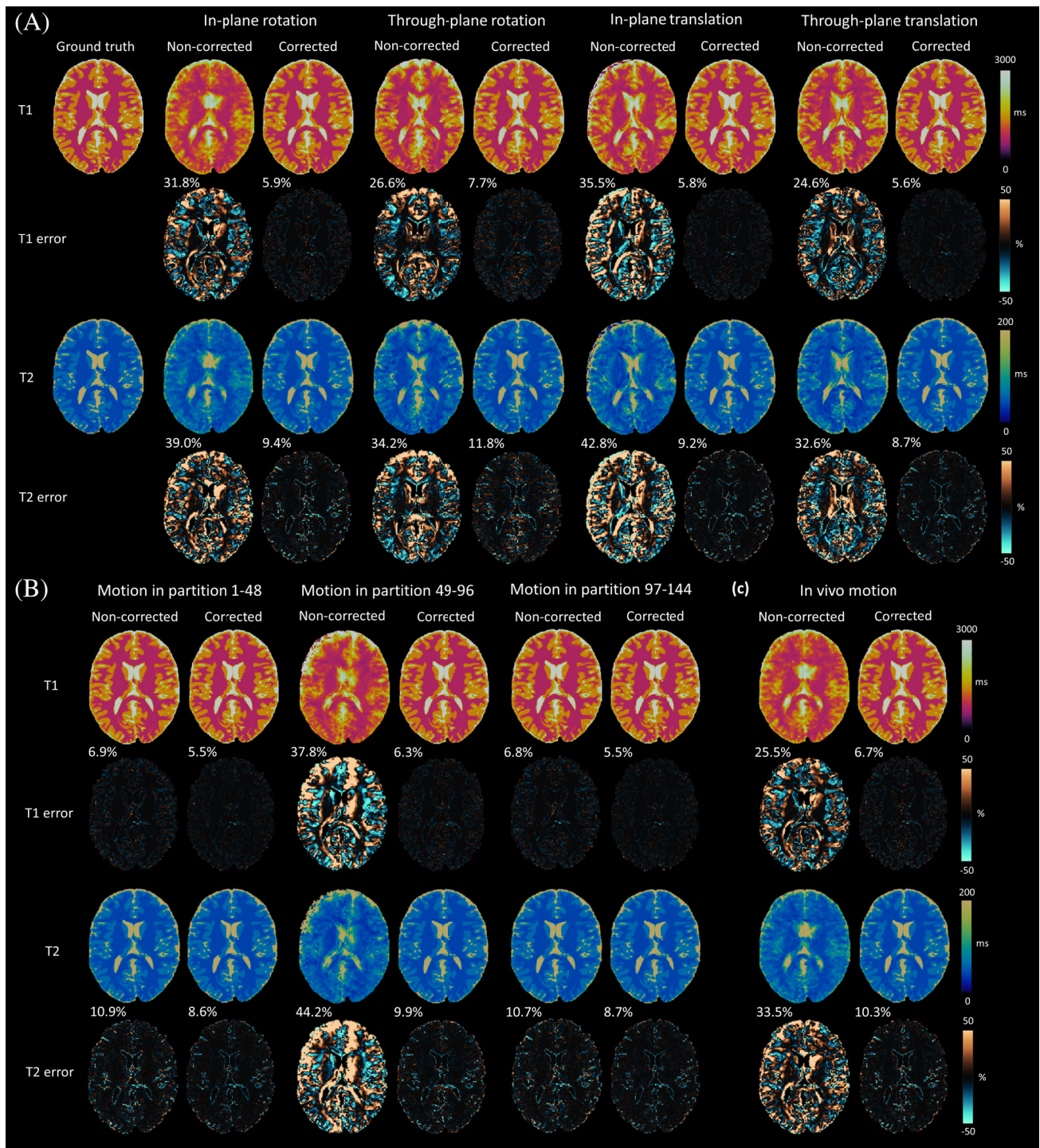
FIGURE 4 Simulated MRF maps, corresponding error maps, and percentage RMS errors compared against the ground truth before and after correction in the three simulation studies. (A) Various types of motion (in-plane/through-plane rotation/translation) were applied. Sharp edges were blurred after rotation; translational motion caused both blurring and ghosting artifacts. (B) Motion at different times. Motion in the first or the last partitions only caused minimal artifacts. Motion in the center partitions played dominant role in inducing motion-related artifacts. (C) In vivo motion applied. These artifacts could be effectively reduced after motion correction.

both T1 and T2 maps. T2 mapping was more vulnerable to motion than T1 for all the motion types. These artifacts resulted in RMS errors of up to 35.5% for T1 and 42.8% for T2. These errors were significantly reduced to 5.9%,

7.7%, 5.8%, and 5.6% for T1; 9.4%, 11.8%, 9.2%, and 8.7% for T2 after the correction. The residual errors were likely introduced by partial volume effects, non-uniform Fourier transform, and undersampling.

Figure 4B shows the MRF maps corrupted by motions that occurred at different timings during the acquisition, as well as their motion-corrected MRF maps. Since the 3D MRF is acquired sequentially along the z-direction in the k-space, motion in the first part or the last part of the scan only affects the outer k-space. These caused slight alternations near the brain boundaries, leading to 6.8% and 6.9% errors in T1, and 10.9% and 10.7% errors in T2. When the motion was present in the central partitions, the corrupted k-space center gave rise to large artifacts, resulting in a 37.8% error of T1 and 44.2% error of T2. In the case of using actual in vivo motion in the simulation (Figure 4C), severe blurring could be observed, producing 33.5% and 25.5% errors in T1 and T2. Such errors could be effectively reduced to 6.7% and 10.3%, respectively, after the motion correction.

3.4 | In vivo experiments

T1 and T2 maps obtained with and without motion correction from a representative healthy volunteer performing various kinds of motion throughout the scans are presented in Figure 5 along with an example measured motion curve (the rest of the motion curves and MRF maps at other slices are shown in Figure S4). A maximum movement of ± 5 mm and a rotation angle of $\pm 10°$ was observed for natural motions of shaking, nodding, and rolling within the head coil for normal adults (Figure S4B). Evident blurring was observed on the MRF maps with shaking motions. Nodding and rolling motions produced significant ghosting artifacts around the ventricles and blurring of gray matter structures, especially on T2 maps. The motion artifacts were substantially mitigated after the motion correction based on the waveforms extracted from the fat navigator images.

The pixel-wise quantitative comparison between the reference motion-free MRF maps versus the non-corrected and corrected MRF maps of the representative subject (shown in Figure 5) is presented in Figure 6. The ICCs of non-corrected MRF maps versus the reference were all below 0.5 for both T1 and T2, indicating poor reliability. Motion corrections significantly raised the ICC of shaking, nodding, and rolling motions to 0.77, 0.65, and 0.72 for T1, respectively, showing good correlations with the reference; the ICC of T2 of 0.65, 0.54, and 0.57 were
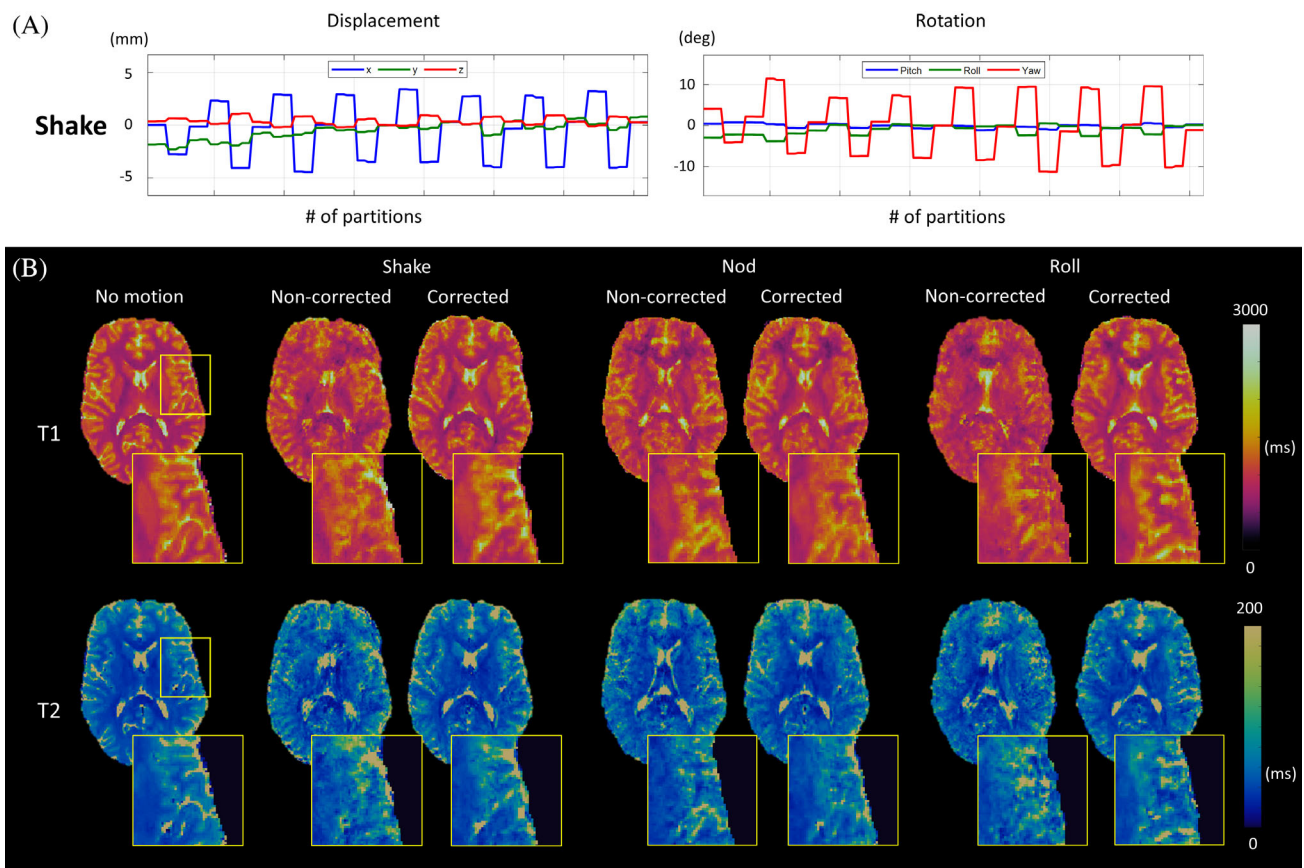

FIGURE 5 (A) An example of estimated in vivo motion curve from a representative volunteer performing shaking. (B) The resulting MRF maps before and after motion correction from scans with motion of shaking, nodding, and rolling. Severe blurring and ghosting artifacts similar to those observed in simulations corrupted the brain structures before motion correction. Image quality was restored after correction.
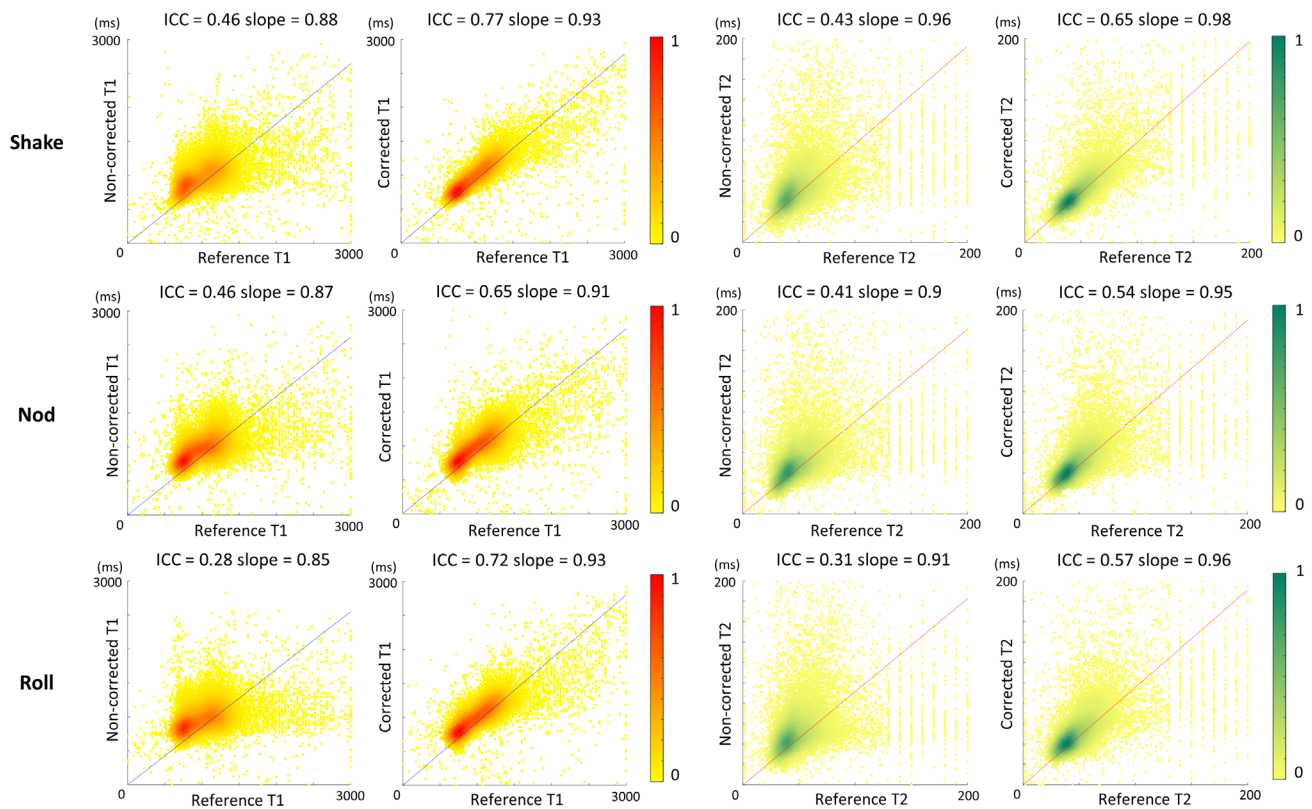
FIGURE 6 Pixel-wise comparison of T1 and T2 values between the reference (no motion) MRF scan and the non-corrected/corrected MRF maps of the representative volunteer at the middle slice. The scatter plots are color coded with normalized local density. ICC were calculated to quantify the similarities. Motion-corrected MRF maps show a significantly higher correlation with the reference.

slightly lower for these three types of motions, yet yielding improved correlations with the reference after motion correction. The results of the pixel-wise analysis for all five volunteers are shown in Figure 7. Different ranges of motion from different scans caused intra-subject variability of the performance of the 3D MRF scans before motion correction (motion signals from each subject were shown in Figure S5). Consistent improvements in ICC for both T1 and T2 after motion correction were observed in all the cases. The ICC of T1 was usually higher than that of T2 after motion correction, which suggests motion correction is overall more effective for T1 mapping than T2 mapping.

Figure 8 shows the in vivo MRF results from a volunteer performing motion at various timings during the acquisitions as well as the extracted motion signals. The MRF maps from the scans where the first 1/3 and the last 1/3 part of acquisitions were affected show minimal motion-related artifacts despite the large motion occurrences; whereas the MRF maps obtained with motion in the center 1/3 partitions were subject to severe blurring and ghosting. These findings were further proved in the pixel-wise quantitative analysis (Figure S6). The results matched the observations in the simulation study that the

motion-induced artifacts in 3D MRF were dominated by the motions that occurred during the acquisition of middle partitions.

The results of ROI-based analysis of T1 and T2 values measured from the motion-corrected MRF scans as compared to the reference values obtained from the motion-free MRF scans for all volunteers are summarized in Table 1. For each individual volunteer, the relaxation times of white matter and gray matter measured from the motion-corrected MRF scans showed no substantial difference from the reference values. The averaged T1 and T2 values across the five volunteers obtained from the motion-corrected MRF maps were all within 2 SDs of the reference values for all ROIs, indicating minimal difference. The variance of T1 and T2 measurements of different volunteers in the motion-corrected MRF maps were comparable with that of motion-free scans, suggesting consistent performance of the motion correction algorithm.

4 | DISCUSSION

In this study, a fat navigator was integrated with 3D MRF to effectively improve the motion robustness of MRF scans in
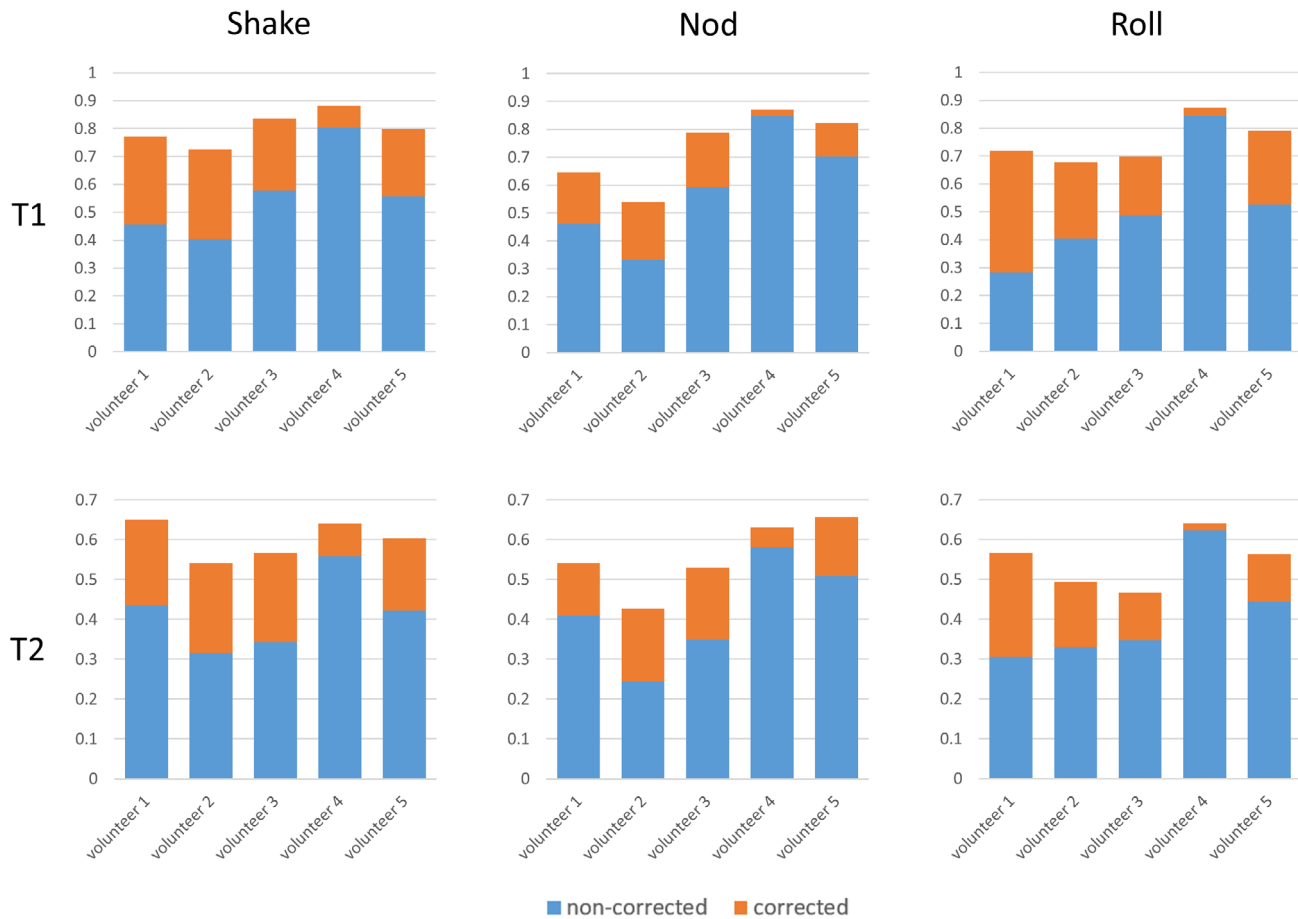
FIGURE 7 ICC of T1 and T2 measurements before and after motion correction for all five volunteers. Blue bars denote the ICC between the non-corrected MRF maps and the reference; orange bars show the improvements in the ICC values after motion correction. Correction is effective across all volunteer scans.

neuroimaging. In combination with non-Cartesian spiral GRAPPA, a rapid fat navigator sampling (approximately 0.5 s) was achieved at 3T, reducing the sensitivity of fat navigator acquisitions to potential motions. The improvement in motion robustness was achieved without increasing the scan time for the 3D MRF acquisition. Our phantom and in vivo results demonstrate that (1) the added fat navigator acquisition led to $2.4 \pm 1.4\%$ difference for T1 and $1.8 \pm 1.4\%$ for T2, indicating minimal influence on the quantification accuracy, and (2) the motion robustness for quantitative tissue mapping using MRF was significantly improved with the proposed method.

In this study, we developed a method to improve the motion robustness of 3D MRF by leveraging motion waveforms extracted from fat images. These images were acquired during the waiting period of the 3D MRF scan, similar to the approach used in the MPRAGE method.[13] Although the Bloch equation simulations used to generate the MRF dictionary were performed based on water signal and the effect due to the acquisition of fat images was neglected in this study, both our phantom and in

vivo results demonstrate that accurate tissue quantification can still be achieved when the fat navigator module was applied at the beginning of the 2-s waiting period. The slight measurement differences might be caused by the partial excitation of water signals by the imperfect fat-selective RF pulse. This problem could be further eliminated by employing a longer binomial chain of RF pulses to obtain more a precise excitation band, but with a trade-off of a longer acquisition time; alternatively, modeling the effect of fat navigator on water signals in the dictionary is another solution. While the effect of small head motion that happened during the acquisition of each partition can be partially compensated with the template matching algorithm, it is difficult to eliminate the large head motion as shown in Figure 5. The in vivo results suggest that the developed method can effectively mitigate motion artifacts introduced by various bulk motions with six degrees of freedom. As head motion is the most problematic and relevant to pediatric imaging, we also demonstrated a promising application of the proposed method on an infant with neonatal opioid
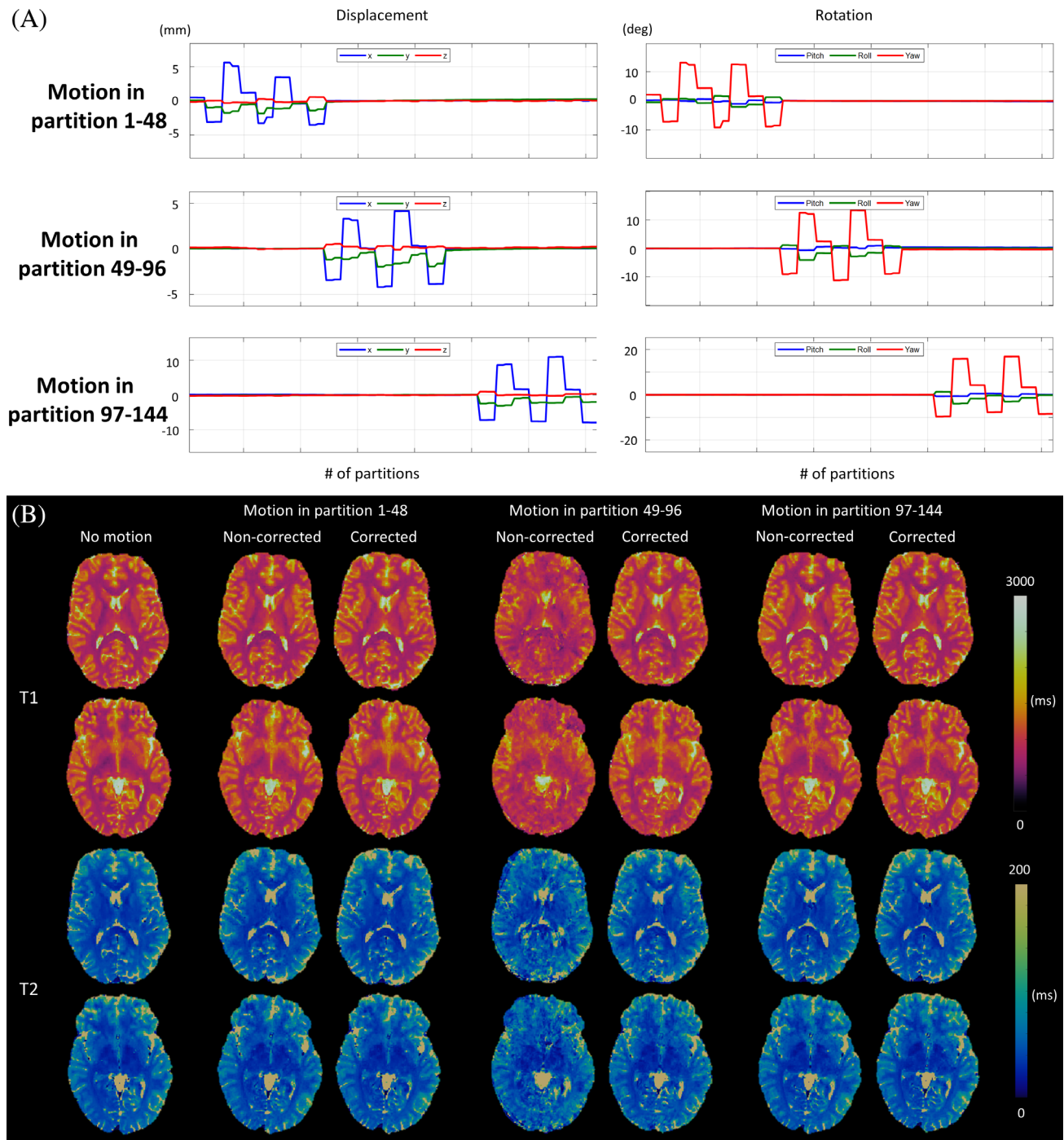
FIGURE 8 (A) Estimated in vivo motion curve from the representative volunteer performing shaking at different time intervals during the scan. (B) The resulting MRF maps before and after motion correction. Only the motion occurring during the acquisition of the center partitions caused significant blurring without motion correction, validating the observations in the simulations.

withdrawal symptoms. The results verified the potential of the 3D MRF scan with fat navigators for pediatric applications.

In the simulations, we demonstrated different motion schemes yielded different motion-related errors in 3D MRF measurements (Figure 4). In the presence of bulk motion in between partitions, combining signals corrupted by motions leads to inconsistent k-space data. Because 3D MRF utilizes Cartesian encoding in the partition encoding direction, the inconsistencies caused the motion-related artifacts to spread along all partitions, independent of the direction of motion. In the simulation, sinusoidal movements caused periodic signal modulation, which resulted in ghosting artifacts. Misregistration of

TABLE 1 T1 and T2 values in five volunteers from the motion-corrected MRF scans with shaking, nodding, and rolling motions versus the reference values from the motion-free scans

		Volunteer 1	Volunteer 2	Volunteer 3	Volunteer 4	Volunteer 5	Mean ± Std
WM T1	No motion	754	768	780	753	801	771.2 ± 17.9
	Shake	735	775	754	774	738	755.2 ± 17.0
	Nod	776	785	783	772	793	781.8 ± 7.3
	Roll	761	732	805	786	765	769.8 ± 24.6
WM T2	No motion	42.3	42.1	40.6	42.1	39.9	41.4 ± 1.0
	Shake	41.3	38.6	36.7	40.7	43.3	40.1 ± 2.3
	Nod	41.8	43	39.5	42	39.9	41.2 ± 1.3
	Roll	43.8	42.8	42.3	40.4	44.2	42.7 ± 1.3
GM T1	No motion	1292	1280	1316	1390	1363	1328.2 ± 42.0
	Shake	1255	1266	1378	1395	1377	1334.2 ± 60.6
	Nod	1256	1314	1300	1351	1337	1311.6 ± 33.0
	Roll	1308	1267	1264	1350	1341	1306.0 ± 35.9
GM T2	No motion	60.2	64.3	62.6	60	57.2	60.9 ± 2.4
	Shake	61.1	64.8	59.4	60.8	59.5	61.1 ± 2.0
	Nod	58.4	56.4	58.6	58.8	58.6	58.2 ± 0.9
	Roll	64.9	60.1	57.7	58	64.5	61.0 ± 3.1

signals from false k-space positions led to mixing of signals of multiple tissues and gave rise to blurring of sharp edges. Both effects could be observed on in vivo MRF maps (Figure 5). Among the various types of motions, in-plane rotations and translations induced slightly higher errors than through-plane motions when the applied motions were on the same magnitude (Figure 4A), since the 3D k-space data volume became more distorted with in-plane motion by geometry. For most types of motions, correction by directly aligning the k-space was helpful. However, it was less effective to correct through-plane rotations (Figure 4A), since rotating the trajectory coordinates in the partition direction could produce gaps in k-space, resulting in residual artifacts due to the ill-posed low-rank reconstruction. Similar trend could also be observed in in vivo data (Figures 6 and 7), nodding and rolling motions that involved through-plane rotations often made the motion correction algorithm more difficult to eliminate the artifacts. Additionally, the timings of motion occurrence also impacted the quality of MRF mapping (Figures 4 and 8). With the sequential sampling ordering along z-direction, acquisition of the center k-space data was concentrated at the middle time interval. We showed that the 3D MRF scans were robust if motion occurred during the sampling of outer k-space.

With the current 3D MRF protocol, each set of fat images was acquired every 7 s to correct bulk motion. However, it is possible to insert multiple fat navigator modules during the acquisition of MRF data for each partition to increase the sampling frequency for motion measurement.[26] In this case, Bloch equation simulations need to be modified to take into account the influence of the fat navigator in the dictionary for accurate tissue quantification. On the other hand, it is possible to accelerate the data acquisition of each partition in 3D MRF. The MRF scans in this study were acquired using an optimized sequence pattern with 480 time frames,[27] which took 5 s to sample each partition (excluding the waiting period). The scans could be further shortened with appropriate sequence design and advanced reconstruction methods, such as deep learning-based methods[28–30] and low-rank matrix completion-based methods with constraints in the Fourier domain.[31,32] These methods can be combined with the proposed method to increase the sampling frequency of the fat navigator to further improve the motion robustness of 3D MRF.

Sliding window methods have been developed to improve motion robustness for MRF as mentioned in the introduction. Since MRF data are generally highly-undersampled, k-space data from multiple time frames are combined to extract motion information for retrospective correction in 2D MRF. With spiral sampling, the motion waveform can be updated every 0.2–0.3 s dependent on the imaging protocol, yielding effective motion correction in 2D acquisitions. However, it is challenging to apply similar approaches for the 3D MRF framework

implemented in this study, where the stack-of-spirals trajectory is used to sequentially acquire k-space data along the partition direction. Recently, 3D MRF using 3D spiral projection trajectory has been developed and the method has demonstrated certain motion tolerance with the template patching algorithm, similar to the original 2D MRF method.[33] The 3D spiral projection trajectory traverses the center k-space in every shot for all partitions and enables self-navigation methods including sliding window reconstruction to improve motion robustness of 3D MRF. This provides an alternative approach to improve the performance of 3D MRF without influencing high scan efficiency. Comparing the two encoding strategies, 3D MRF acquisitions with stack-of-spirals are only sensitive to motion incurred at certain timings during the scan as shown in Figure 8. For 3D spiral projection trajectory, motion present at any time could potentially affect the image quality. The proposed fat navigator can be implemented in both cases and any MRF sampling schemes with non-cubic FOV to achieve maximum scan efficiency.

There are some limitations in the current study. First, the developed method was well suited for bulk motion at a relatively low temporal resolution of every 7 s. The effectiveness of the fat-navigator-based motion correction for motions that occur faster than the acquisition frequency of fat navigator, such as continuous motion, was also evaluated in additional simulations and in vivo studies (see more details in Figure S8–S10). The results from both simulations and in vivo scans demonstrate the proposed method could still reduce the motion-artifacts on MRF map in the presence of the long-persisting high-frequency motion, but there exists a baseline of motion speed that leads to failure of the proposed method. In real-life scenarios, the fast and periodical continuous movements are the less common cases as compared to slow continuous motion, such as drifting or occasional changes of head poses. But, to capture such high-frequency motion that exists within the acquisition of a partition, it requires fat navigators to be acquired more frequently during MRF acquisition and consider the effect of fat navigator in dictionary simulation. Second, the method was not performed on a broad subject base. Only normal subjects with intentional motion were evaluated. Future work will focus on translational studies in clinical settings with pediatric populations.[34]

5 | CONCLUSIONS

In conclusion, we developed a 3D MRF method in combination with a rapid fat navigator to improve its motion robustness for quantitative neuroimaging. Our results demonstrate that (1) accurate tissue quantification was preserved with the additional fat navigator modules and (2) the motion robustness for quantitative tissue mapping using MRF was largely improved in the presence of large head motions with the proposed method.

ORCID
Siyuan Hu https://orcid.org/0000-0003-3137-0605

TWITTER
Siyuan Hu @MRI_Dan

REFERENCES
1. Zaitsev M, Akin B, LeVan P, Knowles BR. Prospective motion correction in functional MRI. *Neuroimage.* 2017;154:33-42. doi:10.1016/j.neuroimage.2016.11.014
2. Ma D, Gulani V, Seiberlich N, et al. Magnetic resonance fingerprinting. *Nature.* 2013;495:187-192.
3. Gao Y, Chen Y, Ma D, et al. Preclinical MR fingerprinting (MRF) at 7 T: effective quantitative imaging for rodent disease models. *NMR Biomed.* 2015;28:384-394.
4. Mehta BB, Ma D, Pierre EY, Jiang Y, Coppo S, Griswold MA. Image reconstruction algorithm for motion insensitive MR fingerprinting (MRF): MORF. *Magn Reson Med.* 2018;80:2485-2500.
5. Cruz G, Jaubert O, Schneider T, Botnar RM, Prieto C. Rigid motion-corrected magnetic resonance fingerprinting. *Magn Reson Med.* 2019;81:947-961. doi:10.1002/mrm.27448
6. Yu Z, Zhao T, Assländer J, Lattanzi R, Sodickson DK, Cloos MA. Exploring the sensitivity of magnetic resonance fingerprinting to motion. *Magn Reson Imaging.* 2018;54:241-248. doi:10.1016/J.MRI.2018.09.002
7. Xu Z, Ye H, Lyu M, et al. Rigid motion correction for magnetic resonance fingerprinting with sliding-window reconstruction and image registration. *Magn Reson Imaging.* 2019;57:303-312. doi:10.1016/j.mri.2018.11.001
8. Kurzawski JW, Cencini M, Peretti L, et al. Retrospective rigid motion correction of three-dimensional magnetic resonance fingerprinting of the human brain. *Magn Reson Med.* 2020;84:2606-2615. doi:10.1002/mrm.28301
9. Pirkl CM, Cencini M, Kurzawski JW, et al. Learning residual motion correction for fast and robust 3D multiparametric MRI. *Med Image Anal.* 2022;77:102387. doi:10.1016/J.MEDIA.2022.102387
10. Skare S, Hartwig A, Mårtensson M, Avventi E, Engström M. Properties of a 2D fat navigator for prospective image domain correction of nodding motion in brain MRI. *Magn Reson Med.* 2015;73:1110-1119. doi:10.1002/MRM.25234
11. Engström M, Mårtensson M, Avventi E, Norbeck O, Skare S. Collapsed fat navigators for brain 3D rigid body motion. *Magn Reson Imaging.* 2015;33:984-991. doi:10.1016/J.MRI.2015.06.014

12. Chen Y, Zong X, Ma D, Lin W, Griswold M. Improving motion robustness of 3D MR fingerprinting using fat navigator. *29th Proc Intl Soc Mag Reson Med*. International Society for Magnetic Resonance in Medicine; 2020. Abstract # 0871.

13. Gallichan D, Marques JP, Gruetter R. Retrospective correction of involuntary microscopic head movement using highly accelerated fat image navigators (3D FatNavs) at 7T. *Magn Reson Med*. 2016;75:1030-1039. doi:10.1002/mrm.25670

14. Gallichan D, Marques JP. Optimizing the acceleration and resolution of three-dimensional fat image navigators for high-resolution motion correction at 7T. *Magn Reson Med*. 2017;77:547-558. doi:10.1002/mrm.26127

15. Ma D, Jiang Y, Chen Y, et al. Fast 3D magnetic resonance fingerprinting for a whole-brain coverage. *Magn Reson Med*. 2018;79:2190-2197. doi:10.1002/mrm.26886

16. Ma D, Jones SE, Deshmane A, et al. Development of high-resolution 3D MR fingerprinting for detection and characterization of epileptic lesions. *J Magn Reson Imaging*. 2019;49:1333-1346. doi:10.1002/jmri.26319

17. Hamilton JI, Jiang Y, Chen Y, et al. MR fingerprinting for rapid quantification of myocardial T1, T2, and proton spin density. *Magn Reson Med*. 2017;77:1446-1458. doi:10.1002/mrm.26216

18. Chen Y, Lee GR, Wright KL, Griswold MA, Seiberlich N, Gulani V. Free-breathing liver perfusion imaging using 3D through-time spiral GRAPPA acceleration. *Invest Radiol*. 2015;50:367-375.

19. Seiberlich N, Lee G, Ehses P, Duerk JL, Gilkeson R, Griswold M. Improved temporal resolution in cardiac imaging using through-time spiral GRAPPA. *Magn Reson Med*. 2011;66:1682-1688.

20. Heidemann RM, Griswold MA, Seiberlich N, et al. Direct parallel image reconstructions for spiral trajectories using GRAPPA. *Magn Reson Med*. 2006;56:317-326. doi:10.1002/mrm.20951

21. Fessler JA, Sutton BP. *Nonuniform Fast Fourier Transforms Using min-Max Interpolation*. Vol 51; 2003:560-574.

22. Friston KJ, Ashburner J, Frith CD, Poline J-B, Heather JD, Frackowiak RSJ. Spatial registration and normalization of images. *Hum Brain Mapp*. IEEE Transactions on Signal Processing; 1995;3:165-189.

23. McGivney DF, Pierre E, Ma D, et al. SVD compression for magnetic resonance fingerprinting in the time domain. *IEEE Trans Med Imaging*. 2014;33:2311-2322. doi:10.1109/TMI.2014.2337321

24. Hamilton JI, Jiang Y, Ma D, et al. Simultaneous multislice cardiac magnetic resonance fingerprinting using low rank reconstruction. *NMR Biomed*. 2019;32:e4041. doi:10.1002/NBM.4041

25. Lo WC, Bittencourt LK, Panda A, et al. Multicenter repeatability and reproducibility of MR fingerprinting in phantoms and in prostatic tissue. *Magn Reson Med*. 2022;88:1818-1827. doi:10.1002/mrm.29264

26. Moore J, Jimenez J, Lin W, Powers W, Zong X. Prospective motion correction and automatic segmentation of penetrating arteries in phase contrast MRI at 7 T. *Magn Reson Med*. 2022;88:2088-2100. doi:10.1002/mrm.29364

27. Jordan SP, Hu S, Rozada I, et al. Automated design of pulse sequences for magnetic resonance fingerprinting using physics-inspired optimization. *Proceedings of the National Academy of Sciences of The United States of America*. Vol 118; Proceedings of the National Academy of Sciences; 2021. doi:10.1073/PNAS.2020516118/-/DCSUPPLEMENTAL

28. Song P, Eldar YC, Mazor G, Rodrigues MRD. Magnetic resonance fingerprinting using a residual convolutional neural network. *ICASSP 2019–2019 IEEE International Conference on Acoustics, Speech and Signal Processing (ICASSP)*; ICASSP 2019 - 2019 IEEE International Conference on Acoustics, Speech and Signal Processing (ICASSP); 2019:1040-1044. doi:10.1109/ICASSP.2019.8682622

29. Oksuz I, Cruz G, Clough J, et al. Magnetic resonance fingerprinting using recurrent neural networks. *2019 IEEE 16th International Symposium on Biomedical Imaging (ISBI 2019)*; 2019 IEEE 16th International Symposium on Biomedical Imaging (ISBI 2019); 2019:1537-1540. doi:10.1109/ISBI.2019.8759502

30. Fang Z, Chen Y, Liu M, et al. Deep learning for fast and spatially constrained tissue quantification from highly accelerated data in magnetic resonance fingerprinting. *IEEE Trans Med Imaging*. 2019;38:2364-2374. doi:10.1109/TMI.2019.2899328

31. Doneva M, Amthor T, Koken P, Sommer K, Börnert P. Matrix completion-based reconstruction for undersampled magnetic resonance fingerprinting data. *Magn Reson Imaging*. 2017;41:41-52. doi:10.1016/j.mri.2017.02.007

32. Hu Y, Li P, Chen H, Zou L, Wang H. High-quality MR fingerprinting reconstruction using structured low-rank matrix completion and subspace projection. *IEEE Trans Med Imaging*. 2022;41:1150-1164. doi:10.1109/TMI.2021.3133329

33. Cao X, Ye H, Liao C, Li Q, He H, Zhong J. Fast 3D brain MR fingerprinting based on multi-axis spiral projection trajectory. *Magn Reson Med*. 2019;82:289-301.

34. Chen Y, Chen MH, Baluyot K, Potts T, Jimenez J, Lin W. MR fingerprinting enables quantitative measures of brain tissue relaxation times and myelin water fraction in early brain development. *Neuroimage*. 2019;186:782-793.

SUPPORTING INFORMATION

Additional supporting information may be found in the online version of the article at the publisher's website.

Figure S1. Motion waveforms of the simulation studies. (A) various types of motion: in-plane rotation (1st row), through-plane rotation (2nd row), in-plane translation (3rd row), and through-plane translation (4th row). (B) Motion occurrences at different time intervals. (C) actual motion waveforms extracted from a preliminary in vivo scan.

Figure S2. In vivo validation of quantitative accuracy of the fat-navigator 3D MRF scan. (A) T1 and T2 maps obtained from a healthy volunteer with and without the fat navigator module during the 3D MRF acquisition. (B) Results of the ROI-based analysis. The locations of the three ROIs are labeled using blue circles in (A).

Figure S3. Example ROIs drawn on a representative volunteer for Table 1.

Figure S4. (A) Non-corrected and motion-corrected MRF maps at difference slices from the motion scans as compared to the reference scan without motion, and (B) corresponding motion waveforms for each type of motion.

Figure S5. Motion waveforms estimated from the rest of the normal subjects in the in vivo experiments. (A)–(D) show the motion waveforms from the 4 volunteers respectively. While subject 3 in (C) performed significant drifting motion, all other volunteers moved head positions in a sinusoidal pattern.

Figure S6. Pixel-wise analysis of in vivo MRF maps obtained with motion during different times of the scan. T1 and T2 values between the reference (no motion) MRF scan and the non-corrected/corrected MRF map at the middle slice were compared. The MRF scan acquired with motion in the middle partitions showed significantly lower similarity to the reference for both T1 and T2.

Figure S7. (A) T1 and T2 maps, synthetic T1-w and T2-w images from the 3D MRF as compared to the real T1-w and T2-w images from the clinical scans obtained with motions of shaking. (B) Extracted motion signals from the 3D MRF scan with motion. The clinical scans were subject to severe artifacts in the presence of motion, making them unreadable. The synthetic MR images yielded significantly improved image quality.

Figure S8. Motion waveforms used in the simulation study of continuous motion, including 4 types of motion (in-plane rotation, through-plane rotation, in-plane translation, and through-plane translation), each at three frequency levels (1/10, 1/6, and 1/3 cycle per 7 s).

Figure S9. Simulated MRF maps and the percentage RMSE compared with the reference brain phantom before and after correction in the continuous motion simulation study.

Figure S10. (A) In vivo motion waveform from the healthy volunteer continuously performing shaking at two different speeds throughout the MRF scans. (B) the resulting MRF maps before and after motion correction.